Editors' Suggestion

VO_2 under hydrostatic pressure: Isostructural phase transition close to a critical endpoint

P. Bouvier,[1,*] L. Bussmann,[1] D. Machon,[2,3,4] I. Breslavetz,[5] G. Garbarino,[6] P. Strobel,[1] and V. Dmitriev[1]

[1]*Université Grenoble Alpes, Institut Néel CNRS, 25 Rue des Martyrs, 38042, Grenoble, France*

[2]*Laboratoire Nanotechnologies et Nanosystèmes (LN2) - CNRS IRL-3463 Institut Interdisciplinaire d'Innovation Technologique (3IT), Université de Sherbrooke, 3000 Boulevard Université, Sherbrooke, J1K OA5 Québec, Canada*

[3]*Institut Interdisciplinaire d'Innovation Technologique (3IT), Université de Sherbrooke, 3000 Boulevard Université, Sherbrooke, J1K OA5 Québec, Canada*

[4]*Université de Lyon, INSA Lyon, CNRS, Ecole Centrale de Lyon, Université Claude Bernard Lyon 1, CPE Lyon, INL, UMR5270, 69621 Villeurbanne, France*

[5]*LNCMI, UPR 3228, CNRS, EMFL, Université Grenoble Alpes, 38000 Grenoble, France*

[6]*European Synchrotron Radiation Facility, BP220, 38043 Grenoble Cedex, France*

(Received 22 June 2023; revised 20 September 2023; accepted 21 September 2023; published 16 October 2023)

The high-pressure behavior of monoclinic VO_2 is revisited by a combination of Raman spectroscopy and x-ray diffraction on a single crystal under hydrostatic conditions at room temperature. A soft mode is observed up to $P_c = 13.9(1)$ GPa. At this pressure, an isostructural phase transition between two monoclinic phases M_1 and M_1' hinders this instability. The features of this transformation (no apparent volume jump) indicate that the compression at ambient temperature passes close to a critical point. An analysis based on the Landau theory of phase transitions gives a complete description of the P-T phase diagram. The M_1' is characterized by spontaneous displacements of the oxygen sublattice without any strong modification of the VV dimers distances nor the twist angle of vanadium chains. The spontaneous displacements of oxygen and the spontaneous deformations of the $(b_{M1},\ c_{M1})$ plane follow the same quadratic dependence with pressure and scales with spontaneous shifts of the Raman phonons located at 225, 260, and 310 cm^{-1}. Pressure-induced shifts of the Raman peaks allow for new assignment of several Raman modes. In particular, the $A_g(1) + B_g(1)$ modes at 145 cm^{-1} are identified as the vanadium displacive phonons. A second transformation in the metallic phase X, which is found triclinic ($P\bar{1}$) is observed starting at 32 GPa, with a wide coexistence region (up to 42 GPa). Upon decompression, phase X transforms, between 20 and 3 GPa, to another phase that is neither the M_1' nor M_1 phase. The structural transitions identified under pressure match with all the previously reported electronic modifications confirming that lattice and electronic degrees of freedom are closely coupled in this correlated material.

DOI: 10.1103/PhysRevB.108.144106

I. INTRODUCTION

VO_2 is a well-known prototypical electron-correlated material, showing a metal-to-insulator transition (MIT) at ambient pressure and moderate temperature $T = 340$ K [1] accompanied with a structural phase transition. Despite VO_2 already being used in a variety of technological applications, such as infrared detection, thermochromics, transistors, or microactuators (see the reviews in Refs. [2–4]), the microscopic mechanism of the MIT is still an open fundamental question and a challenge for finding accurate functionals for theoretical density-functional theory (DFT) calculations [5,6]. Two mechanisms have been proposed and are still debated in many experimental and theoretical studies: the Peierls lattice distortion model and the Mott orbital electron model (or a mixture of both mechanisms) [7–33].

The associated structural transition from the metallic rutile structure ($P4_2/mnm$, No. 136, $Z = 2$ [34]) to the low-temperature insulating monoclinic ($P2_1/c$, No. 14, $Z = 4$ [35]), named M_1, was explained by the phonon condensation at the R point of the rutile Brillouin zone with vanadium displacements as the order parameter (OP) [36,37,10,11,38,39]. Thus, the metallic rutile structure is made of two vanadium chains with equal VV distances whereas the insulating monoclinic phase is characterized by two zigzagging chains with VV dimers. The thermodynamics of this displacive Peierls mechanism and the stability limits of the different phases were described in the framework of a Landau-type phenomenological model with a reduced two-dimensional component OP and free-energy expanded to sixth degree, and eventually coupled with the strain [40–46,32,47]. This phenomenological description predicts the possibility of stabilizing other phases, such as a monoclinic $C2/m$ (No. 12) phase, named M_2, and an intermediate triclinic phase $P\bar{1}$ (No. 2), named T (or M_3) [10,38,39]. These M_2 and T structures were observed in VO_2 doped with cation of lower oxidation states [48–52,45] or under specific uniaxial stress [53,34,54,55,41–43,56–61,46,62]. The MIT was found to be remarkably affected by mechanical stresses [63–65] and a triple point between M_1, M_2, and rutile phases was observed at 340 K at zero strain [40,58].

Applying pressure is a relevant way to modify the stability between structural or electronic degrees of freedom.

*pierre.bouvier@neel.cnrs.fr

 ©2023 American Physical Society

Thus, in M_1 phase of VO_2, spectral discontinuities in both the midinfrared optical conductivity and in the behavior of two Raman-active phonons located at 190 and 225 cm^{-1} [66–69], observed at 10 GPa under quasihydrostatic pressure, were interpreted as vanadium dimer rearrangement [66]. Electrical discontinuity was also reported at 10–13 GPa [70,71]. Synchrotron x-ray-diffraction studies of pure VO_2 powders [72,71,69,73] or nanoparticles [74] have shown that the M_1 phase transforms, above 11–13 GPa, to an isostructural phase (same space group $P2_1/c$ No. 14, $Z = 4$), named M_1'. Since there is no apparent change in the crystal symmetry, the transition pressure is defined by a discontinuity in the compression behavior of the (b_{M1}, c_{M1}) monoclinic plane [72,71,69,74]. Contrary to early studies, Bai *et al.* proposed that the discontinuities measured at the M_1-M_1' transition in the pressure dependence of the Raman modes located at 190, 225, and 320 cm^{-1} are not associated with any V-chain rearrangement [71]. The persistence of the VV dimerization up to 22 GPa and a VV-pair twist angle remaining close to 3° was then confirmed by atomic pair distribution function analysis [75]. Density-functional theory calculations suggested that the M_1-M_1' transition is induced by an unstable Γ-point phonon that is related to the rotation of the oxygen octahedra along the monoclinic a_{M1} axis (or the parent rutile c_R axis) [76]. In their calculations, the pressure-induced reduction of the band gap and metallization is accounted by clockwise rotations (phase M_1'') that progressively reduce the dimerization and zigzags of the vanadium chains [76].

At higher pressure, a second phase transition to a metallic phase X was detected (between 28 and 50 GPa). The slope change [69] or splitting [71] of the Raman mode at 225 cm^{-1}, observed above 27.8 GPa, was assigned to phase X. Afterwards, Balédent *et al.* observed this splitting at 19 GPa and proposed a new insulating M_3 phase, different from the metallic phase X [73]. Different structures have been proposed for phase X such as a monoclinic baddeleyite type ($P2_1/c$, No. 14) with $Z = 8$ [71,69] or with $Z = 4$, named M_x [74,77] in which the vanadium coordination number increases from 6 to 7. Xie *et al.* proposed that a different seven-coordinated orthorhombic structure ($Pmn2_1$, No. 31, $Z = 2$) coexists with the low-pressure M_1 between 29 and 79 GPa [78]. A different monoclinic space group (Pn, No. 7) was inferred using spin-polarized *ab initio* structure search [73]. Under decreasing pressure, another monoclinic baddeleyite-type polymorph, named M'_x, was reported following a high-pressure treatment of the M_1 phase up to 63 GPa [74,77]. Additional pressure measurements, at 383 K [71], or on W-doped VO_2 [79], have shown that rutile phase transforms at 13.3 GPa to an orthorhombic $CaCl_2$-type structure ($Pnnm$, No. 58, $Z = 4$) and coexists with metallic phase X between 32 and 64 GPa. The pressure-temperature phase diagram of VO_2 was built using Raman, optical reflectance, and electrical transport characterizations [80].

Therefore, although many experimental and theoretical calculations were published concluding on the presence of several different M_1', M_1'', M_3, phase X, M_x, and M'_x structures under increasing pressure, no agreement has yet been reached on the phase sequence under high pressure and on the associated mechanisms. One of the reasons lies in the experimental limitation due to the form of the sample (powder, nanobeams) and quasi hydrostatic conditions that can play a significant role. The aim of this study is to present results obtained by Raman and x-ray-diffraction analysis on a high-quality VO_2 single crystal compressed under hydrostatic conditions using helium as the pressure-transmitting medium. In a first Sec. III A, x-ray-diffraction data obtained during compression will be displayed. These make it possible to clarify the phase-transition sequence and the microscopic mechanism involved. Then in Sec. III B, Raman spectroscopy measurements will be presented with insights in terms of assignment and pressure-induced behavior. A phenomenological analysis will be proposed to describe the experimental P-T phase diagram of VO_2 in Secs. IV A and IV B. In the last Sec. IV C, the obtained results are combined to correlate the behaviors of the Raman modes with the strains and microscopic characteristics of the compound. This will be of interest to characterize phases in thin films of (doped) VO_2 and the nature and amplitude of the strains.

II. EXPERIMENT

High-quality crystals with natural faces of stoichiometric VO_2 crystals were produced by chemical vapor transport, using $TeCl_4$ transport agent and following the procedure described in Ref. [81].

High-pressure experiments were performed using a membrane-driven diamond-anvil cell (DAC) with 250/300-μm beveled diamond culets. A pressure chamber of 160 μm in diameter and 40 μm in thickness was drilled in a stainless-steel gasket. Helium, loaded at 1.4 kbar, was used as the pressure-transmitting medium to ensure high hydrostatic pressure conditions up to 42 GPa, the highest pressure reached in this study. During the Raman experiment, the pressure was measured using the R_1-line emission of a ruby ball placed close to the sample using Holzapfel equation of state [82]. The ruby signal was measured before and after each measurement in order to control the pressure drift during long acquisitions. The recorded pressure was set at the average of these two pressure values and the uncertainty is set as half of the difference between these two values. The homogeneity of the pressure in the DAC was followed from both the width and the splitting between the R_1 and R_2 ruby lines [83,84]. During the x-ray-diffraction experiment, the pressure was measured using the equation of state of pure copper powder [85] placed close to the crystal. The copper x-ray-diffraction images were integrated with DIOPTAS software [86].

Three experiments on two different single crystals were done. During the first one, we recorded only Raman on a crystal of 40 × 30 μm in size and 10 μm in thickness up to 42 GPa and back to room pressure. We have reproduced this Raman experiment on a smaller crystal of 15 × 18 μm in size and 10 μm in thickness up to 25 GPa and back to room pressure. During this second experiment, we have chosen not to exceed 25 GPa in order to avoid forming the high-pressure metallic phase. A third experiment up to 35 GPa, using x-ray-diffraction was done with the second crystal that had already experienced pressure during the second Raman experiment.

The ruby and Raman measurements were made at room temperature using a 514.4-nm laser (Cobolt Fandango) and a 750-mm spectrometer (SP2750, Acton Research) with a 2400-

grooves per millimeter grating (blazed at 500 nm), equipped with a cooled charge-coupled camera (PyLoN, Princeton), and a 50-μm entrance slit size that provides a resolution of 0.70 cm^{-1} (0.019 nm). A set of Bragg filters (BNF-Opti grate) was used in order to reject the excitation line. The spectra were recorded in backscattering geometry with a 50× objective (Nikon) to focus the incident laser beam and collect the scattered light from inside the DAC through the diamond anvil. The spectrometer was calibrated in wave number using the lines of a Ne-Ar lamp. The incident laser power was fixed at 0.5 mW (measured before the DAC) in order to avoid any laser heating of the sample that could induce the M_1-rutile transition at 340 K. The Raman spectra covering a 25–900-cm^{-1} spectral range were recorded using two monochromator positions with a maximum of 300-s acquisition time averaged over two to four acquisitions. In the 25–150-cm^{-1} range, we have subtracted the contribution of N_2/O_2 rotations lines. Spectral parameters (position and full width at half maximum were obtained from the decomposition of each spectrum with several Lorentzian peaks using FITYK software (version 1.3.1) [87].

Single-crystal x-ray-diffraction (XRD) experiment was done at ID15B beamline (ESRF Grenoble) with a monochromatic wavelength $\lambda = 0.41020$ Å and a $2 \times 4-\mu m$ focused beam. Diffraction images were collected during the continuous rotation of the DAC around the vertical ω axis in a range $\pm 32^\circ$, with an angular step of $\Delta\omega = 0.5^\circ$ and an exposure time of 0.5 s per frame. The CRYSALIS^{pro} software package [88] was used for the analysis of the single-crystal XRD data (indexing, data integration, frame scaling, and absorption correction). A single crystal of Vanadinite [$Pb_5(VO_4)_3Cl$, *Pbca* space group, $a = 8.8117(2)$ Å, $b = 5.18320(10)$ Å, and $c = 18.2391(3)$ Å] was used to calibrate the instrumental model in the CRYSALIS^{pro} software, i.e., the sample-to-detector distance, detector's origin, offsets of the goniometer angles, and rotation of both the x-ray beam and detector around the instrument axis. Using the JANA2006 software package, the structure was solved with the SHELXT structure solution program [89]. Crystal-structure visualization was made with the VESTA software [90]. The equation of state (EoS) was obtained by fitting the pressure-volume data using a third-order Birch-Murnaghan (BM EoS). Le Bail profile analyses of the pattern measured at 35 GPa were carried out using the FULLPROF software [91]. Cell parameters and overall thermal factor were refined. The background was first removed with a spline interpolation and then refined as a linear function. The peak shape was described with pseudo-Voigt function. The profile parameters u, v, w and the mixing parameter of the pseudo-Voigt function were kept fixed for the final refinement.

III. RESULTS

A. Single-crystal x-ray diffraction under high pressure

The single-crystal diffraction measured in the restricted geometry of the DAC allows to index 180 peaks (~30% of the total reciprocal lattice) in a monoclinic reduced Niggli cell with $a_{M1} = 5.3548(6)$ Å, $b_{M1} = 4.5253(2)$ Å, $c_{M1} = 5.3817(3)$ Å, $\beta_{M1} = 115.224(9)^\circ$, and volume $V_{M1} = 117.974(15)$ Å^3 with space group $P2_1/c$ (No. 14, $Z = 4$, cell choice 1). Notice that this reduced cell is identical to the $P2_1/n$ (No. 14, $Z = 4$, cell choice 2) monoclinic cell with $a_{M1} = 5.7510(8)$ Å, $b_{M1} = 4.5253(17)$ Å, $c_{M1} = 5.3548(6)$ Å, and $\beta_{M1} = 122.16(2)^\circ$, in agreement with the lattice parameters reported in the ICSD [35] for phase M_1. The reciprocal maps attest to the absence of multidomains in the crystal measured under pressure (see Fig. S1 in the Supplemental Material (SM) [92]). Unfortunately, the orientation of the crystal in the DAC was not favorable to access the [0*k*0] direction in the (*hk*0) plane and to confirm the presence of the 2_1-screw axis along the *b* axis. However, the specific extinctions (*h*0*l*) with $h + l = 2n$ and (*h*00) with $h = 2n$ due to the presence of a mirror *n* perpendicular to the *b* axis are observed. The crystallographic extinctions are not modified up to 34 GPa (Fig. S2 in the SM [92]) which discard any structural transition to $P\bar{1}$ (No. 2), $P2_1$ (No. 4), or *Pc* (No. 7) subgroups of the $P2_1/c$ space group. The diffraction intensities are refined in the M_1 phase (see the refinement parameters at 0.3 GPa in Table S1 in the SM [92]). The crystallographic parameters (unit-cell parameters, volume, and atomic positions) up to 34 GPa are given in Table S2 in the SM [92].

Figures 1(a)–1(d) display the monoclinic unit-cell parameters evolution with increasing pressure. As observed previously [72,71,69,74], the a_{M1} lattice parameter decreases without any detectable discontinuity between 0 and 34 GPa, whereas above 13–14 GPa, a discontinuity is observed in the (b_{M1}, c_{M1}) monoclinic plane, i.e., the b_{M1} softens while the c_{M1} hardens simultaneously. A discontinuity is also observed in the pressure behavior of the beta angle at 14 GPa [see Fig. 1(c)]. The nonlinear pressure dependence of cell parameters is reproduced by a third-order Birch-Murnaghan–like equation of state (BM EoS) with $a^\circ_{M1} = 5.7506(7)$ Å, $K^\circ = 545(5)$ GPa, and $K' = 4.9(3)$ between 0 and 34 GPa and by three second-order BM-like EoS with $b^\circ_{M1} = 4.5259(7)$ Å, $K^\circ = 630(9)$ GPa, $c^\circ_{M1} = 5.3521(12)$ Å, $K^\circ = 820(23)$ GPa and $\beta^\circ = 122.16(1)^\circ$, $K^\circ = 12672(682)$ GPa between 0 and 13 GPa. Below 14 GPa, the monoclinic a_{M1} cell parameter is more compressible than the b_{M1} and c_{M1} parameters and the beta angle is remarkably stiff. Using the EoS of the low-pressure M_1 and extrapolating them above 14 GPa, the elastic spontaneous deformations e_{11}, e_{22}, e_{33}, e_{12}, e_{13}, e_{23}, and the $e_{\text{total}} = \sqrt{(\sum e_{ij}^2)}$ are calculated in the high-pressure monoclinic phase. The e_{11}, e_{12}, e_{13}, and e_{23} stay at values close to zero, whereas the e_{22}, e_{33}, and e_{total} increase as the square root of $(P - P_c)$ as shown in Fig. 2. Maximum values of $e_{22} = -1.5\%$, $e_{33} = +2.5\%$, and $e_{\text{total}} = +2.9\%$ are reached at 34 GPa.

The pressure dependence of the volume shown in Fig. 3(a) did not show any obvious discontinuity in the whole pressure range. The volume variation was first fitted with one unique third-order BM EoS with $V_0 = 117.97(4)$ Å^3, $K^\circ = 214(2)$ GPa, and $K' = 2.5(1)$ between 0 and 34 GPa. However, the value of K' less than 4 and the discontinuity at 13–14 GPa in the $F-f$ plot reveal the structural transition [see inset in Fig. 3(a) using $V_0 = 117.97$ A^3]. Thus, the EoS of M_1 phase are $V_0 = 118.00(4)$ A^3, $K^\circ = 194(7)$ GPa, and $K' = 7(1)$ between 0 and 14 GPa and $V_0 = 119.6(6)$ A^3,

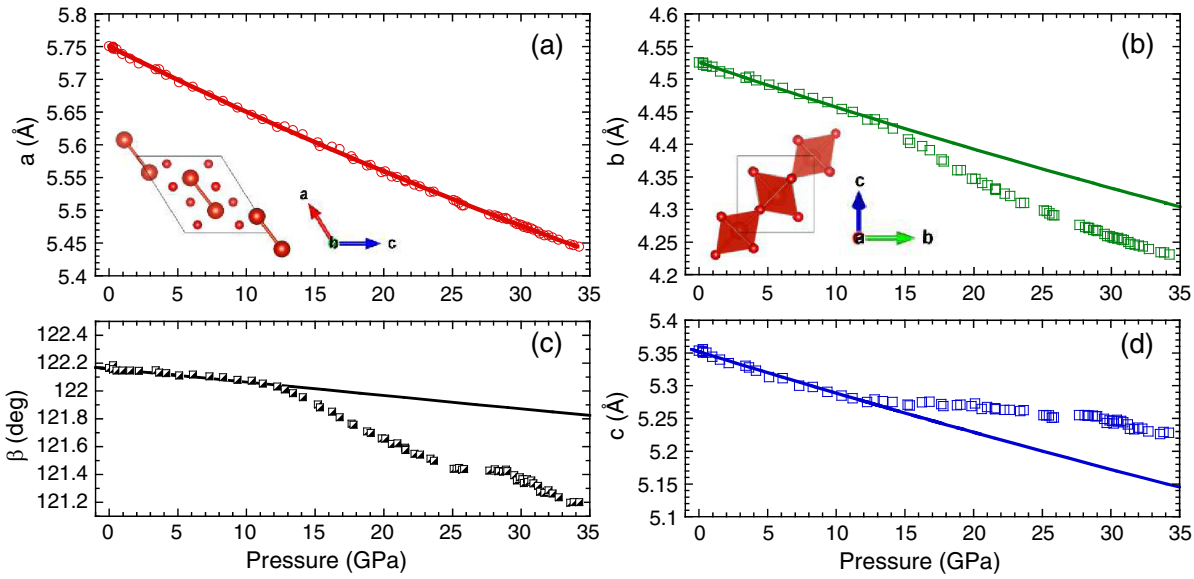

FIG. 1. VO_2 monoclinic cell parameters with increasing pressure; (a) a_{M1} axis, (b) b_{M1} axis, (c) β angle between a_{M1} and c_{M1}, and (d) c_{M1} axis in M_1 phase $P2_1/n$ cell choice 2. Full lines correspond to BM EoS between 0 and 34 GPa (see text). Inset in (a) shows VV dimers along monoclinic a_{M1} axis. Inset in (b) shows VO_6 octahedra in (b_{M1}, c_{M1}) plane.

$K^\circ = 162(17)$ GPa, and $K' = 4.6(8)$ between 14 and 34 GPa. The EoS of M_1 and M_1' phases agree with Ref. [71]. The K° values are 15% lower than those measured on nanoparticles [74]. The distance between the two vanadium atoms of VV dimers along the monoclinic chain shows a regular decrease with pressure from 2.62 to 2.47 Å at 34 GPa [see Fig. 3(b)] and is fitted by a third-order BM-like EoS with $d^\circ_{VV} = 2.6199(8)$ Å, $K^\circ = 564(14)$ GPa, and $K' = 2.3(8)$. A maximum contraction of 5.7% is measured at 34 GPa. As shown in Fig. 3(c), the VO_6 polyhedra reduce their volume without any apparent discontinuity at 14 GPa and can be reproduced by a third-order BM EoS with $V^\circ_{octa} = 9.542(6)$ Å^3, $K^\circ = 173(5)$ GPa, and $K' = 12.2(7)$. A maximum contraction of 10% is measured at 34 GPa. The individual VO distances inside an octahedron, reported in Fig. S3 in the SM [92], show a regular decrease with the tendency for the VO_6 polyhedron to become more symmetric.

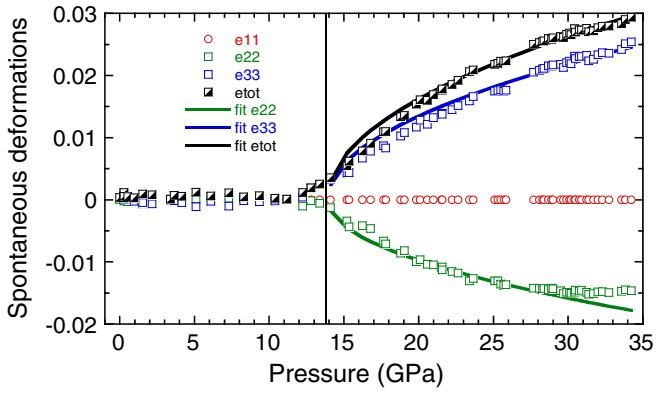

FIG. 2. Spontaneous deformations calculated in high-pressure monoclinic cell against original low-pressure monoclinic M_1 using EoS extrapolated above 14 GPa. Full lines are square-root functions with $(P - P_c)$ with fixed $P_c = 13.9$ GPa.

The relative variations of the atomic fractional parameters with pressure obtained from refining the single-crystal diffraction intensities indexed in space group $P2_1/n$ (No. 14, $Z = 4$, cell choice 2) are reported in Fig. 4. Vanadium and oxygen atoms are in general position (site 4*e*). The vanadium coordinate along b_{M1} increases continuously by 0.4(1)% at 34 GPa. They decrease by 0.3(1)% at 14 GPa in the (a_{M1}, c_{M1}) plane and remain constant above. The two oxygen fractional positions almost do not change in the pressure range 0–14 GPa, but they display a clear deviation above 14 GPa that is one order of magnitude larger than that of the vanadium displacements. In Fig. 4(b), we report the spontaneous displacements of both oxygens atoms measured along the three crystallographic directions after subtracting the displacements extrapolated from the behavior below 14 GPa. Notice that both oxygen atoms display opposite spontaneous displacements of the exact same amplitude along a_{M1} (former c_R axis in the rutile phase) and c_{M1} directions while they move in the same direction along b_{M1} (former a_R axis in the rutile phase). The oxygen spontaneous displacements follow a square-root dependence with $P - P_c$ with fixed $P_c = 13.9$ GPa as plotted with plain lines in Fig. 4(b).

At 35 GPa, the previous well-resolved single-crystal diffraction pattern disappeared suddenly. The crystal is damaged, which indicates a first-order transition. Some crystallographic axes are still observed; however, Bragg peaks are spread in the azimuthal direction (see inset in Fig. 5). Different structural models (including baddeleyite-type phase X from Ref. [71], M_x from Refs. [74,77], or orthorhombic phase from Ref. [78]) were tested but none of them could reproduce the x-ray-diffraction pattern. The pattern was indexed with a triclinic ($P\bar{1}$) cell with $a = 9.075(3)$ A, $b = 4.412(2)$ A, $c = 4.996(3)$ A, $\alpha = 87.84(4)^\circ$, $\beta = 94.52(4)^\circ$, $\gamma = 92.67(4)^\circ$, and $V = 199.05(19)$ A^3 with Bragg R factor of 0.4% as

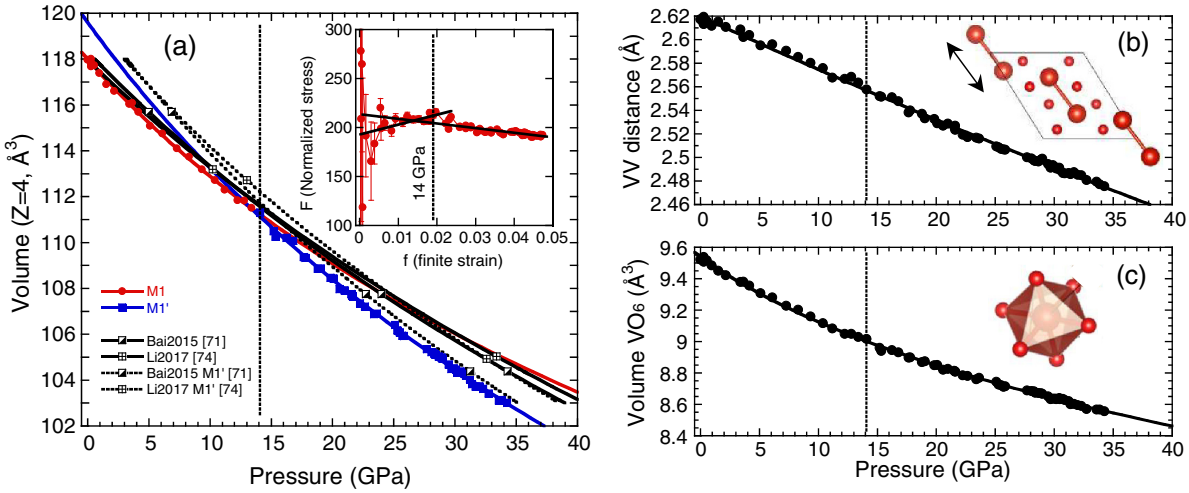

FIG. 3. VO_2 monoclinic parameters with increasing pressure (a) volume for $Z = 4$ and F-f plot in inset; (b) vanadium distances inside VV dimers, and (c) volume of VO_6 polyhedron. Full lines correspond to third-order BM EoS. Others EoS from previous works are reported for comparison.

reported in Fig. 5. The unit cell contains height VO_2 formula unit. A volume jump of $\Delta V/V = -3.3(1)$ % is measured at the transition. The high-pressure phase X is different from the structural model reported for the triclinic phase in VO_2 doped with cation of lower oxidation states or under uniaxial stress. If it was the case, we would expect a second-order continuous transition that is not observed. Attempts were made to refine the structure starting from a baddeleyite-type model but the statistics in azimuthal direction was not good and the intensity was too low to obtain a reliable refinement.

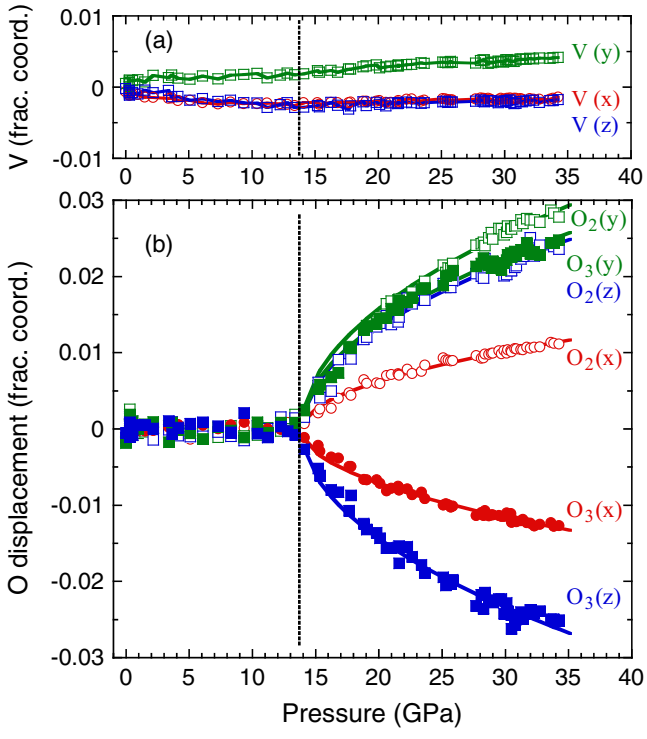

FIG. 4. Pressure dependence of (a) vanadium fractional coordinates $V(x) + 0.712$, $V(y) - 0.478$, and $V(z) + 0.473$ and (b) fractional oxygen displacements measured after subtracting displacements extrapolated from behavior below 14 GPa in space group $P2_1/n$ (No. 14, $Z = 4$, cell choice 2). Full lines in (b) are square-root function with $(P - P_c)$ with fixed $P_c = 13.9$ GPa.

B. Single-crystal Raman spectra under high pressure

The Raman spectrum measured on a VO_2 single crystal is identical to previously published spectra for the M_1 phase [93–98]. Eighteen Raman-active modes ($9A_g + 9B_g$) were expected and almost all of them were identified at 83 K on a naturally oriented single crystal [94,95] (Table I). Figure 6 displays a zoom on the low wave number part of the Raman spectra (70–340 cm^{-1}) to highlight the softening/hardening of the low-lying 145-cm^{-1} weak mode observed under pressure. The Stokes and anti-Stokes spectra measured at 21 GPa (see Fig. S5 in the SM [92]) confirm that this mode is a phonon and not a fluorescent artifact. The entire Raman spectra measured up to 25 GPa are reported in Fig. S4 in the SM [92]. In this

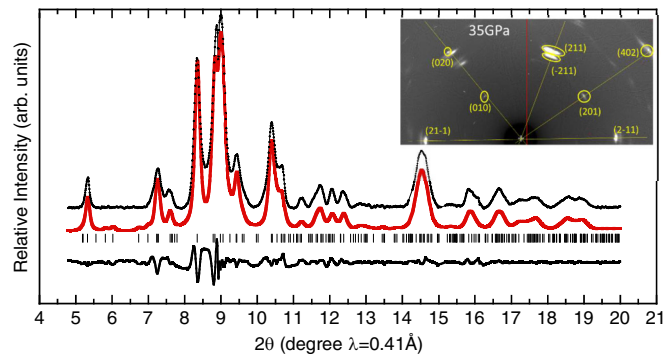

FIG. 5. Result of Le Bail profile fitting in triclinic $P\bar{1}$ unit cell at 35 GPa for phase X. Expected diffraction peaks are indicated by ticks. Difference between experimental and fit is reported at bottom. Inset shows two-dimensional image of crystal with tentative indexation.

TABLE I. Position in wave number (cm^{-1}) of Raman-active modes measured experimentally or calculated for monoclinic M_1 phase of VO_2 and symmetry assignment propositions from literature. Lines in dark gray or light gray highlight the A_g or B_g symmetry of Raman modes. Stars ***, **, * indicate Raman intensity from most intense to less intense.

Position (cm^{-1})	[93]	[94]	[95]	[17]	[96]	[99] calc.	[97]	[98]	[100] calc.	Monoclinic M_1 This work
** 145	-	-	A_g	B_g	-	A_g	B_g	A_g+B_g	A_g	$A_g(1)$+$B_g(1)$
*** 190	A_g	A_g	A_g	A_g	A_g	A_g+B_g	A_g	A_g	A_g+B_g	$A_g(2)$
*** 225	A_g	A_g	A_g	A_g	A_g	A_g+B_g	A_g	A_g+B_g	A_g+B_g	$A_g(3)$+$B_g(3)$
* 260	A_g	B_g+B_g	B_g+B_g	-	-	B_g+B_g	B_g	B_g	B_g	$B_g(2)$
** 310	A_g	A_g	A_g	-	B_g	A_g	A_g	A_g	A_g	$A_g(4)$
340	A_g	B_g	B_g	-	A_g	A_g	A_g	A_g	A_g+B_g	$B_g(4)$
** 390	A_g	A_g	A_g	-	A_g	A_g	A_g	A_g	A_g	$A_g(5)$
** 394	-	B_g	B_g	-	-	B_g	B_g	B_g	-	$B_g(5)$
440	Ag	B_g	B_g	-	-	B_g	B_g	B_g	B_g	$A_g(6)$
445	-	B_g	A_g	-	-	B_g	B_g	-	B_g	$B_g(6)$
485	-	B_g	B_g	-	-	B_g	B_g	B_g	B_g	$B_g(7)$
500	A_g	A_g	A_g	-	A_g	A_g	A_g	A_g	A_g	$A_g(7)$
** 595	B_g	A_g	A_g	-	-	B_g	A_g	B_g	B_g	$A_g(8)$
*** 615	A_g	A_g	A_g	-	A_g	A_g	A_g	A_g	A_g	$A_g(9)$
665	-	B_g	B_g	-	-	A_g	B_g	A_g	A_g	$B_g(8)$
850	-	B_g	B_g	-	-	B_g	B_g	B_g	B_g	$B_g(9)$

work the Raman modes are labeled as $A_g(1)$ to $A_g(9)$, and $B_g(1)$ to $B_g(9)$ in Fig. 6 and in Fig. S4 in the SM [92].

Figure 7 presents the pressure dependence of spectral parameters obtained from the decomposition of Raman spectra with Lorentzian functions. In the past studies, the symmetry assignment of lowest wave number mode at 145 cm^{-1} was not conclusive (A_g, B_g, or the superposition of both symmetries was proposed) [97,98] (Table I gathers the different assignments proposed in the literature). Here, thanks to the different pressure dependences, we confirm that at ambient conditions, one soft mode and one hard mode with different symmetries are superimposed at 145 cm^{-1}. At pressure above $P_c = 13.9(1)$ GPa, the soft mode changes its behavior and starts hardening, which marks the isostructural M_1-M_1' transition. This transition is reversible with no pressure hysteresis. Extrapolating the $\nu_{SM}^2(P)$ to $\nu_{SM} = 0$ limit gives $P_c^* = 26.9(4)$ GPa, for the potential stability limit of the M_1 phase. The ratio between the slopes $d\nu^2/dP$ below and above P_c is 2.4(1), close to 2, characteristic of a continuous phase transition. With increasing pressure, the hardening mode successively crosses the $A_g(1)$ mode at 25 GPa and the 190-cm^{-1} $A_g(2)$ mode at 29.5 GPa, and shows a deviation from the linear dependence at pressure higher than 32 GPa before disappearing at 41 GPa [Fig. 7(a)]. The spectra recorded between 20 and 29 GPa showing the successive crossing between low wave number modes are reported in Fig. S6(a) in the SM [92]. The pressure evolution of the half width at half maximum (HWHM) of both $B_g(1)$ and $A_g(1)$ modes obtained from the decomposition of the Raman spectra using FITYK software are reported in Fig. S6(b) in the SM [92]. The $B_g(1)$ HWHM is narrower (2 cm^{-1}) than the $A_g(1)$ (6 cm^{-1}). Under pressure, the HWHM of $B_g(1)$ remains constant as $A_g(1)$ decreases sharply. Above 20 GPa, depending on experience and therefore local conditions, HWHM may fluctuate, but as far as positions are concerned, everything is reproducible. The integrated intensity (area) progressively increases with pressure above P_c [Fig. 7(b)]. Contrary to previous studies [66–68,71,73], the $A_g(2)$ mode at 190 cm^{-1} does not show any abrupt increase in the rate $d\nu/dP$ at P_c. We rather measured a small decrease of the slope from $d\nu/dP = 0.36(1)$ to 0.22(1) cm^{-1}/GPa at the transition. The discontinuity reported at 10 GPa in previous studies might be a consequence of the use of nonhydrostatic pressure-transmitting media, i.e., NaCl, KCl [66,67], or ethanol-methanol [68,69,80] that are known to be strongly anisotropic at this pressure. The HWHM [Fig. 7(d)] shows a regular decrease with pressure up to 29 GPa, followed by a tendency to increase that is always observed at such high pressure because of the progressive loss of hydrostaticity of the helium transmitting medium. The same tendency is measured on the ruby pressure marker [see Fig. 7(d)]. The integrated intensity (area) of the $A_g(2)$ peak [Fig. 7(c)] is almost constant up to 32 GPa and suddenly drops at higher pressure before disappearing at 41 GPa. The pressure dependences $d\nu/dP$ and the Grüneisen parameters of the Raman modes are reported in Table II and their positions are given at 0 GPa for the M_1 phase and at 13.9 GPa for the M_1' high-pressure phase.

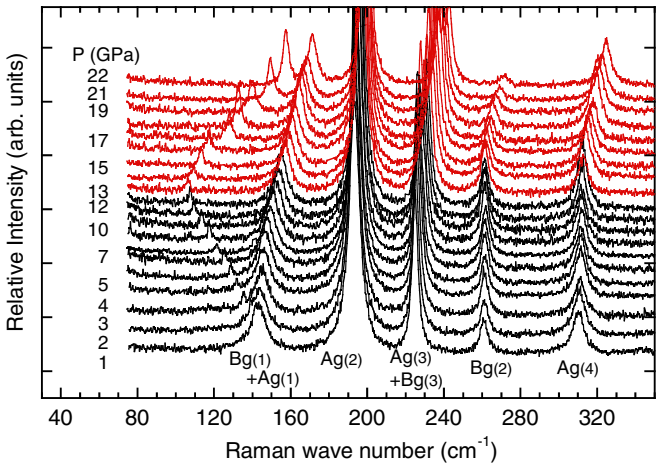

FIG. 6. Low wave number part (70–340 cm^{-1}) of Raman spectra measured on VO_2 single crystal showing softening/hardening of 145-cm^{-1} Raman mode under increasing pressure. Pressures are quoted on left of each spectrum. Black lines correspond to monoclinic M_1 phase. Red lines highlight pressure higher than $P_c = 13.9(1)$ GPa. Symmetry A_g or B_g of each mode is indicated at bottom.

A second original observation in Raman spectra of the M_1 phase under pressure is the splitting of the mode at 225 cm^{-1} in two components at pressure as low as 3 GPa within the resolution limit of our spectrometer [see Fig. 7(a) and Fig. S7 in the SM [92]). This mode was in the past associated with a single A_g symmetry but experimental [98] and theoretical studies [99,100] have proposed that two modes of A_g and B_g symmetries could be superimposed at room condition. Here again, pressure allows for distinguishing both modes due to their different pressure dependences. Both modes show sharp slope changes in $\nu(P)$ at $P_c = 13.9(1)$ GPa (see Table II).

The variations of the spectral features at the transition allow for correlating the Raman modes with the different components of the strain. The spontaneous shift $\nu(M'_1)$-$\nu(M_1)$ is calculated after subtracting the wave number $\nu(M_1)$ extrapolated above P_c from the behavior measured below 14 GPa. The $A_g(3)$ scales linearly with the absolute value $|e_{22}|$ of the spontaneous strain along b_{M1} [Fig. 8(a)] or with $(e_{33}$-$e_{22})$ that

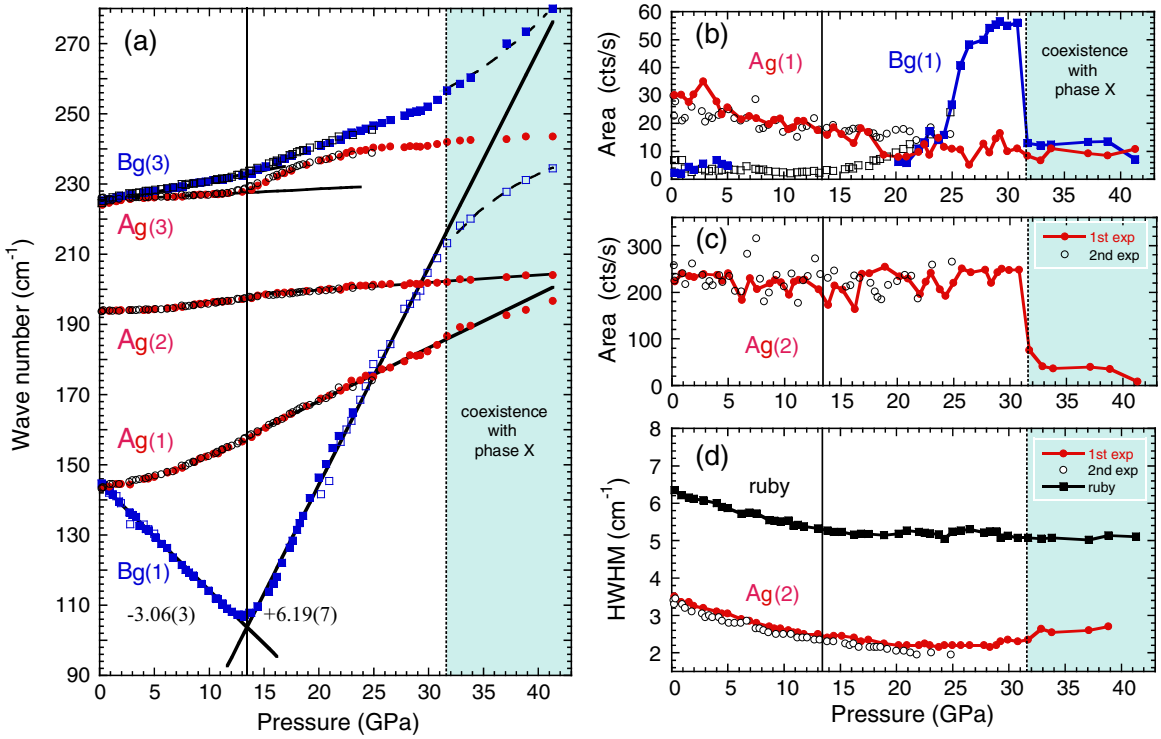

FIG. 7. Low wave number Raman spectral parameters measured under increasing hydrostatic pressure; (a) wave numbers of $A_g(1)$, $B_g(1)$, $A_g(2)$, $A_g(3)$, and $B_g(3)$ modes (see labels in Fig. 6), (b) integrated intensity (area/s) of $A_g(1)$ and $B_g(1)$ modes, (c) integrated intensity (area/s) of most intense $A_g(2)$ mode, and (d) HWHM of $A_g(2)$ mode and of ruby pressure marker. Red and blue colors stand for A_g and B_g symmetry, respectively.

reflects the deformation of the $(b_{M1},\ c_{M1})$ plane. The $B_g(3)$ scales linearly with the square of the spontaneous strain along $c_{M1}(e_{33}^2)$ [see Fig. 8(b)]. With further increasing pressure, at 29 GPa another discontinuity is observed in the splitting (see Fig. S7 in the SM [92]). In previous studies the splitting was observed only above 27–28 GPa [71,69] or above 19 GPa [73] but was associated with phase X or with insulating M_3 phase, different from phase X.

A third original observation in the M_1 phase concerns the Raman modes $B_g(2)$ at 260 cm^{-1} and $A_g(4)$ at 310 cm^{-1}. They exhibit an unusual small pressure dependence of their positions [see Figs. 9(a) and 9(b)]. The slopes are $dv/dP =$

TABLE II. Wave number dependence with pressure for Raman modes in M_1 and M_1' high-pressure monoclinic VO_2. Grüneisen parameter $\Upsilon = (K/v)(dv/dP)_T$. Errors are in parentheses.

Raman-mode symmetry		Position @00GPa (cm^{-1})	Slope (cm^{-1}/GPa)	Grüneisen Υ	Position @13.9GPa (cm^{-1})	Slope (cm^{-1}/GPa)
$A_g(1)$		142.9(2)	+0.77(4)	+1.04(9)	158.9(3)	+1.52(2)
	$B_g(1)$	144.9(2)	−3.06(3)	−4.1(2)	106.4(7)	+6.19(7)
$A_g(2)$		192.5(1)	+0.36(1)	+0.36(2)	198.5(1)	+0.22(1)
	$B_g(3)$	224.6(2)	+0.62(2)	+0.53(4)	233.6(1)	+1.15(1)
$A_g(3)$		225.4(1)	+0.16(1)	+0.14(1)	229.3(2)	+1.10(4)
	$B_g(2)$	261.7(1)	+0.03(1)	+0.022(8)	259.9(2)	+1.50(4)
$A_g(4)$		311.4(1)	+0.13(1)	+0.081(9)	311(4)	+1.81(3)
	$B_g(4)$	340.7(3)	+4.42(4)	+2.52(11)	400.1(4)	+4.06(4)
$A_g(5)$		388.8(3)	+4.06(4)	+2.03(9)	444.1(3)	+2.79(3)
	$B_g(5)$	392.8(5)	+4.32(6)	+2.13(10)	450.7(3)	+2.61(3)
	$B_g(6)$	442				
$A_g(6)$		442.8(3)	+2.35(4)	+1.03(5)	477(1)	+3.15(9)
	$B_g(7)$	483				
$A_g(7)$		499.3(1)	+2.64(1)	+1.03(4)	536.2(2)	+2.02(2)
$A_g(8)$		594.5(8)	+4.37(11)	+1.43(8)	654.5(6)	+2.78(12)
$A_g(9)$		613.4(2)	+3.86(2)	+1.22(5)	668.8(3)	+2.37(3)
	$B_g(8)$	662.8(7)	+2.85(9)	+0.83(5)	703.8	+2.72(7)
	$B_g(9)$					

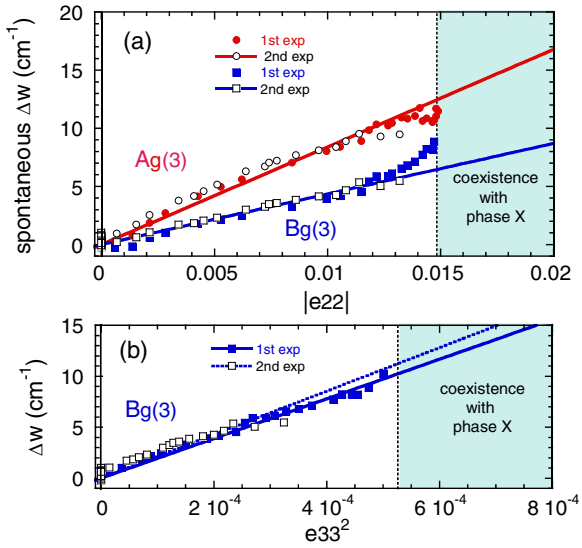

FIG. 8. Spontaneous Raman shift $\nu(M_1') - \nu(M_1)$ after subtracting wave number $\nu(M_1)$ extrapolated above P_c from behavior before $P_c = 14$ GPa: (a) $A_g(3)$ and $B_g(3)$ at 225 cm^{-1} against $|e_{22}|$ spontaneous strain along b_{M1} and (b) $B_g(3)$ at 225 cm^{-1} against e_{33}^2 spontaneous strain along c_{M1}.

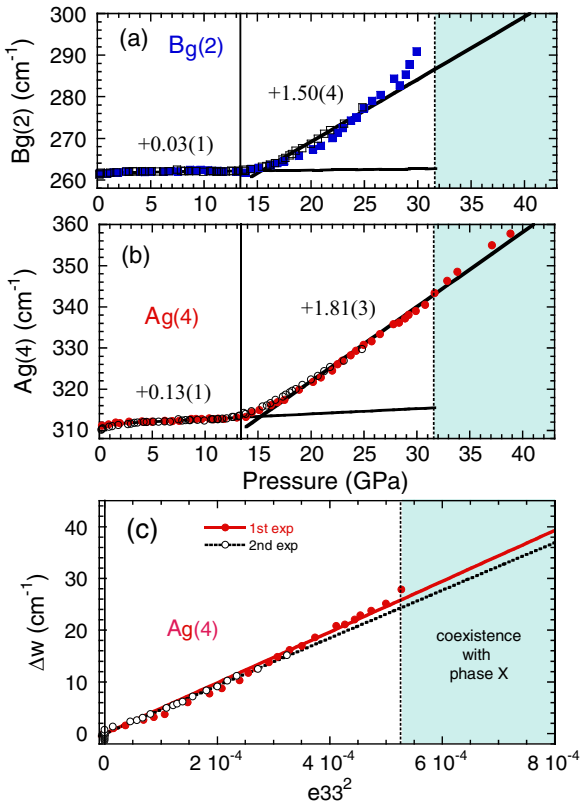

FIG. 9. Wave number of Raman modes measured under increasing hydrostatic pressure on VO_2. (a) $B_g(2)$ at 260 cm^{-1}, and (b) $A_g(4)$ at 310 cm^{-1}. Slopes $d\nu/dP$ are reported in different pressure regions. (c) $A_g(4)$ at 310-cm^{-1} spontaneous Raman shift against e_{33}^2 spontaneous strain along c_{M1}.

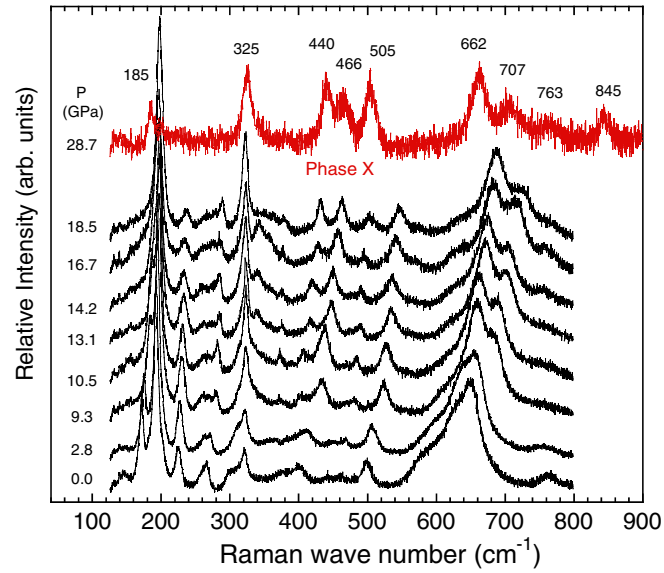

FIG. 10. Raman spectrum measured during decompression from 42 GPa. Signature of phase X (in red at 28.7 GPa) is maintained up to 22 GPa and is transformed to triclinic phase between 22 and 18.5 GPa. Coexistence between both structures is observed up to 3 GPa. Strained triclinic phase is retained at atmospheric pressure and room temperature. Spectra are corrected from linear background.

0.03(1) cm^{-1}/GPa and $d\nu/dP = 0.13(1)$ cm^{-1}/GPa, respectively (see Table II). However, they show an abrupt change in their $d\nu/dP$ at P_c. Some authors have seen that this mode disappears between 14 and 15 GPa [71,69] or at 22 GPa [74]. From our observations, the intensity starts decreasing at 14 GPa but the mode is still observed up to 30 GPa. The slope changes of the $A_g(4)$ mode were reported at the M_1-M_1' transition above 13 GPa [71,74]. The HWHM (not shown) exhibits a regular decrease with increasing pressure similar to that measured on the $A_g(2)$ mode [Fig. 7(b)]. The spontaneous shift $\nu(M'_1) - \nu(M_1)$ for the $A_g(4)$ mode scales linearly with e_{33}^2 [Fig. 9(c)].

The Raman modes at higher wave number exhibit classical increase of their positions with increasing pressure (see Fig. S8 in the SM [92]). The slopes $d\nu/dP$ are larger than those measured for the low wave number modes. A small decrease of the slopes $d\nu/dP$ is observed at P_c (see Table II). Notice that the slope of the $B_g(4)$ mode at 340 cm^{-1} and the $B_g(8)$ mode at 665 cm^{-1} are almost not affected by the transition at P_c.

At 32 GPa, the collapse of the Raman intensity and the sudden increase of the background are the signature of the formation of the metallic phase X. With further increasing pressure up to 41 GPa, the Raman peaks disappear and some other peaks appear progressively. The Raman signature of the pure phase X recorded during decompression is reported in Fig. 10 (in red at 28.7 GPa) and shows nine weak peaks at 185, 325, 440, 466, 505, 662, 707, 763, and 845 cm^{-1} (see Fig. 10 and Fig. S8 in the SM [92]). Upon decompression, the Raman spectra show a transformation, between 22 and 18.5 GPa, to a spectrum of reasonable intensity that is compatible neither with M_1' nor M_1 structures but can be explained by a coexistence between phase X and another structure. The coexistence

persists down to 9.3 GPa but, between 5 and 3 GPa, phase X completely disappears and the remaining spectrum resembles that of the triclinic T phase (or M_3) measured on 0.7% Cr-doped VO_2 by Marini *et al.* [67]. The same signature was reported on VO_2 nanoparticles below 23.9 GPa and down to 2.1 GPa by Li *et al.* [74], and was interpreted as a back transformation from the baddeleyite-type M_X phase into another baddeleyite-type M'_x phase with a local structure similar to the M_1 structure.

IV. DISCUSSION

A. First transition from M_1 to M'_1 at 14 GPa

Depending on the pressure-transmitting medium, the M_1-M'_1 transition has been reported at pressure varying between 10 and 15 GPa [66–68,72,71,74,80]. In our hydrostatic conditions, VO_2 single crystal exhibits a first isostructural transition, M_1 to M'_1, at $P_c = 13.9(1)$ GPa as observed by Raman and x-ray-diffraction measurements. The transition is quasicontinuous, second-order-like with no measurable volume jump. The transition is displacive with oxygen displacements compatible with the R-point condensation (in the parent rutile) without strong modification of the VV dimers nor of the twist angle of vanadium chains (Fig. 4). The oxygen sublattice spontaneous displacements and the spontaneous deformation of the $(b_{M1},\ c_{M1})$ plane follow the same quadratic dependence with pressure (Figs. 2 and 4). The monoclinic a_{M1} lattice parameter is not affected by the transition (Fig. 1).

We can combine these high-quality experimental data with reliable information published so far and suggest therefore a coherent picture of phase transitions in VO_2 compressed and heated/cooled. The rutile to monoclinic transition is an *improper ferroelastic transition of displacive type* and is induced by the four-component order-parameter spanning R_1^- irreducible representation at the R point of the tetragonal Brillouin zone [36,37,10,11,38,39,47]. Mechanical (vibrational) representation of the rutile-type structure at the R point of the Brillouin zone reads

$$T_M = (3R_1^-)_V + (3R_1^- + 3R_1^+)_O. \tag{1}$$

Thus, the symmetry-breaking atomistic mechanism of the structural R-M_1 transformation contains simultaneous vanadium and oxygen atoms displacements, both transforming as R_1^- and, therefore, coupled bilinearly in the free energy. In other words, the symmetry lowering and distortion of the tetragonal structure are controlled by coupled vanadium and oxygen displacements. In the high-temperature rutile phase, the four components of the R_1^- OP are zero: $\eta_1 = \eta_2 = \eta_3 = \eta_4 = 0$, and the vanadium chains are regularly aligned with fixed VV bond distances of 2.86 Å. At the rutile to M_1 transition, one component of the R_1^- OP takes nonzero value $(\eta_1 \neq 0,\ \eta_2 = \eta_3 = \eta_4 = 0)$. The R point imposes that two antiferroelectric vanadium displacements occur when $\eta_1 \neq 0$: one along the a_{M1} axis ($a_{M1} = 2c_R$) forming VV dimers on one chain and one off axis in the plane perpendicular to the a_{M1} axis forming twisted vanadium on the nearest-neighbor vanadium chain [10,47]. Thus if $\eta_1 \neq 0$, two twisted vanadium chains with VV dimers are formed in the M_1 phase.

Under pressure, the second component η_2 of the R_1^- OP, which reduces its symmetry to $B_g(1)$ after the Brillouin-zone folding, drives the structure transformation to the M_2 phase with $\eta_1 = \eta_2 \neq 0$ ($\eta_3 = \eta_4 = 0$). One set of vanadium chain pairs (VV dimers) is not twisted while the other set stays twisted but loses the VV dimers. The M_2 phase is expected at 27 GPa, as estimated from extrapolating the linear part of the soft-mode wave number $\nu^2_{SM}(P)$ measured experimentally to the $\nu_{SM} = 0$ limit. However, the M_2 phase is not observed because the isostructural M_1-M'_1 transition occurs at $P_c = 13.9(1)$ GPa suppressing this instability and conserving the M_1-type phase thermodynamically more stable. The observed phonon softening does not drive the M_1-M'_1 transition (but drives the M_1-M_2). The isostructural transition somehow prevents the M_1-M_2 transition from taking place under hydrostatic pressure as detailed in the Landau-based analysis developed in the next section. The oxygen displacements and the monoclinic $(b_{M1},\ c_{M1})$ plane distortion recall those found in the rutile to $CaCl_2$ transition observed in VO_2 at higher temperature [71,79,80] and in many other AO_2 oxides. However, the oxygen polyhedron is not only rotating along to the a_{M1} axis (former c_R axis in the rutile phase). Let us show, in the framework of phenomenological theory, that the reason for the isostructural transition lies in the highly anharmonic dependence of the free energy on the nontotally symmetric OP.

B. Understanding the VO_2 phase diagram from phenomenological theory

Our experimental findings allow us to derive a complete picture of phase transitions in VO_2 observed under different pressure and temperature conditions ($P < 35$ GPa). This requires to consider two-component effective order parameter. The image group, reduced form of the relevant four-dimensional representation R_1^- to a two-dimensional effective order-parameter group, possesses the point symmetry $4mm$. Phenomenological models for the two-dimensional tetragonal image group were analyzed in detail by Gufan and co-workers and cited in Ref. [101].

The basic invariants forming the integrity basis for the image group $4mm$ are

$$I_1 = \eta_1^2 + \eta_2^2, \text{ and } I_2 = \eta_1^2\eta_2^2. \tag{2}$$

Accordingly, the most compact structurally stable order parameter 10-degree expansion, which is necessary to account for two consecutive first-order phase transitions R-M_1 and M_1-M'_1 (see the Appendix), is expressed as

$$F(\eta_1, \eta_2, P, T) = a_1(P,T)I_1 + a_2(P,T)I_1^2 + b_1 I_2 + c_{12} I_1 I_2 + a_4 I_1^4 + b_2 I_2^2 + a_5 I_1^5. \tag{3}$$

The free-energy equation (3) has four minima corresponding to the four phases known for VO_2:

I: $\eta_1 = \eta_2 = 0 \sim R$;
II: $\eta_1 \neq 0,\ \eta_2 = 0 \sim M_1$;
III: $\eta_1 = \eta_2 \neq 0 \sim M_2$;
IV: $\eta_1 \neq \eta_2 \neq 0 \sim T$.

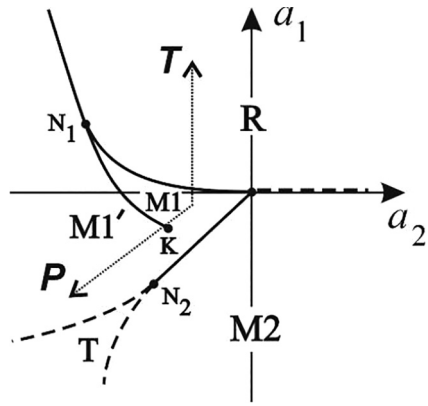

FIG. 11. Equilibrium phase diagram corresponding to free-energy equation (3) in plane of phenomenological coefficients (a_1, a_2) for $0 < a_2 < (c_{12}^2/4b_2)$, $c_{12} < 0$, $a_4 < 8b_2$, $a_5 > 0$. Solid line: first-order; dashed: second-order phase-transition lines. K: critical endpoint; N_1 and N_2 are three-phase points. Pressure (P) and temperature (T) axes are shown schematically.

Figure 11 shows a section of the theoretical phase diagram, corresponding to the potential (3), which is topologically adequate to understand the VO_2 pressure-temperature phases diagram experimentally mapped in hydrostatic conditions. In addition, this free-energy expansion includes the existence of a *critical endpoint* K (gas-liquid type) on the M_1-M_1' transition line at which the first-order transition transforms to a crossover continuous regime (see Appendix, Annex 1). The fact that no apparent volume could be experimentally measured indicates that the isostructural M_1-M_1' transition is quasicontinuous and reveals that the pressure path passes in close vicinity of this critical point K (Fig. 11). Varying pressure at higher temperature should allow to measure an increasing volume jump at the M_1-M_1' transition as one moves away from the critical point. The topology of the phenomenological phase diagram also predicts that the triclinic T structure can be observed at even higher hydrostatic pressures. On the contrary, M_2 and rutile R phases might hardly be formed under hydrostatic pressure at ambient temperature. The phase diagram explains also that Cr-doped VO_2, which adopt triclinic (for 0.7% Cr) or M_2 (for 2.5% Cr) phases, are reported to first transform to M_1 phase at 2.7 and 3.7 GPa, respectively, and then to the same M_1' phase as pure VO_2 at 12 GPa [67,72].

It is worth stressing that the general form of Eq. (3) and the diagram shown in Fig. 11 are generic ones since they also account for stress/strain effects. Indeed, we can distinguish two types of strain components: (i) through improper spontaneous strains induced by the primary order parameter R_1^- (e_{11}, e_{22}, e_{33}, e_{12}, and e_{13}), and (ii) through external deviatoric stress (e_{23}) developing under quasihydrostatic compression conditions, or surface effects in thin films, for instance [41–43]. Although the coupling terms in the free energy have different forms, $\eta_i^2 e_{jk}$ and $\eta_i^2 e_{lm}^2$, they should be integrated with the unique quadratic invariant I_1 in the free-energy equation (3). This will lead to renormalizing the corresponding coefficient $(a_1 + c_{ij} + c_{il}) \rightarrow \tilde{a}_1$ but without modifying the general form of Eq. (3). The topology of the phase diagram of Fig. 11 remains unchanged; however, the transition line can be shifted and then the M_2 phase could be observed under nonhydrostatic stress. Topology means the correct description of the phases in contact, and prediction of the order for the phase transition that can occur between them.

The changes in the midinfrared transmittance/reflectance [66–69] and in the resistivity observed previously under pressure [71,70,80] are concomitant with the M_1-M_1' isostructural transition. This strongly suggests that electronic properties and structural modifications (with oxygen displacements) are linked and that the Peierls mechanism is valid. We can assume that this isostructural transition can also be induced by uniaxial/biaxial stresses in thin films, or in nonstoichiometric VO_2 for which internal stresses can be generated. Thus, experimental studies that have questioned the Peierls mechanism because of the observation of a monoclinic-like metallic VO_2 where electronic and structural transitions seem decoupled [102–105] did not consider the possibility of having formed the isostructural M_1' phase.

C. Raman signature of M_1, M_2, or T phases as a tool for thin-film engineering

The technological interest in VO_2 has led to the study of various thin films or nanobeams using Raman spectrometry as a valuable tool to differentiate between rutile, M_1, M_2, or T phases [106,55,45,57,107–109,45,98,30,110]. The metallic rutile has a weak signal composed of broad modes at 300 and 550 cm^{-1} (for $A_{1g} + B_{1g} + E_g$) [111] that are difficult to measure. The Raman signature of M_1 is quite well documented but not all the $9A_g$ and $9B_g$ modes were observed and the symmetry assignments are still being debated (see Table I). The present study, thanks to pressure-induced variations of the peak positions, allows for clarifying the assignment (see Sec. III B). Moreover, very little is known on the atomic displacements (eigenvectors) involved in each mode. Since the Raman study under oxygen isotopic substitution [67], it is often said that the two intense low wave number modes at 190 and 225 cm^{-1} involve predominantly vanadium displacements. This was supported by the phonon density of state obtained with *ab initio* calculations [112,99,113,100,6,114]. There is a widespread belief that these modes are associated with the stretching and twisting features of the dimerized chains and contribute to the M_1-rutile transition [17,67,112,99,69,100]. However, these modes do not obviously soften at the MIT [93,13,95]. The Raman signature of the T phase is similar to that of M_1 but the $A_g(1)$ mode is downshifted to 126 cm^{-1}, the $A_g(2)$ is upshifted to 200 cm^{-1}, and a small splitting of the $A_g(3) + B_g(3)$ is observed [67,45,107,115–118]. In the M_2 phase, the $A_g(1)$ mode downshifts even more to 50 cm^{-1}, the $A_g(2)$ stays at 200 cm^{-1}, and two components are clearly observed for the $A_g(3) + B_g(3)$ [67,106,55,45,57,107,109,117]. We do not endorse the fact that the $A_g(1)$ mode could be a breathing mode of spin-Peierls dimerized 1D spin-1/2 Heisenberg chain [117] but rather found that the two modes $A_g(1) + B_g(1)$ at 145 cm^{-1} are the vanadium displacive modes expected from the condensation of the rutile R_1^- OP. The progressive softening of the $A_g(1)$ mode through M_1 to T and M_2 structural transformation, where one-half

of the the Peierls pairing and twisting is partially removed or with increasing pressure, where only one mode softens until the transition to M_1' hinders this instability, supports our finding.

The splitting of the $A_g(3) + B_g(3)$ mode, at 225 cm^{-1}, in both M_1 and M_1' phases, highlighted in Fig. 7(a) and Fig. S7 in the SM [92], was often misunderstood in the past. Several DFT calculations concluded that the zigzag V motions that untwist the VV pairs are located between $\sim$ 6.0 THz (197 cm^{-1}) [99], 6.38 THz (213 cm^{-1}) [112], or $\sim$ 6.5 THz (217 cm^{-1}) [119], close to the positions of the $A_g(3) + B_g(3)$ modes. We do not observe any softening with pressure and doubt that these modes are linked to the pairing or tilting motions of VV dimers. We found that the splitting is observed in the M_1 phase at 2–3 GPa [Fig. 7(a)]. Indeed, from the linear pressure evolution of each mode, we found that the two modes intersect at 1.9 GPa, confirming they have different symmetries. The angular dependence of the Raman intensity in different polarized conditions measured outside the DAC, as shown in Fig. S9 in the SM [92], also shows the superimposition of two different symmetries already in the M_1 monoclinic phase at ambient conditions, in agreement with Shibuya *et al.* [98]. The splitting is equal to 0.8 cm^{-1} in the M_1 at room condition, which explains why it was hardly detectable in past studies. At the M_1-M_1' isostructural transition, both modes display an abrupt change of their $d\nu/dP$ [see Fig. 7(a) and Fig. S7 in the SM [92] or in Table II). We found that the $A_g(3)$ scales linearly with the spontaneous strain along b_{M1}, whereas the $B_g(3)$ scales linearly with the square of the spontaneous strain along c_{M1} [see Figs. 8(a) and 8(b)]. Thus, the $A_g(3) + B_g(3)$ splitting is a good marker of the nature of the strain experienced by VO_2. The unusual pressure behavior observed at 24–25 GPa [see Fig. 7(a) and Fig. S7 in the SM [92]) is a consequence of the saturation of the spontaneous deformation along the b_{M1} axis while the one along the c_{M1} increases without there being a phase transition. Quantification of the monoclinic deformation can also be done using either the $A_g(4)$ mode at 310 cm^{-1} or the $B_g(2)$ mode at 260 cm^{-1}. In the M_1 stability region, below P_c, both modes are insensitive to hydrostatic compression [see Figs. 9(a) and 9(b)] and accurate wave number measurements beyond the possible drifts of the equipment can be done using the $B_g(2)$ mode as an internal reference. Above P_c, the $A_g(4)$ scales linearly with e_{33}^2 [see Fig. 9(c)] or e_{total}^2 (not shown), whereas the $B_g(2)$ scales linearly with e_{33}^4 or e_{total}^4.

The high wave number modes, $B_g(4)$ at 340 cm^{-1} (see Fig. S11 in the SM [92]) or $B_g(8)$ at 665 cm^{-1} (not shown), scale linearly with the monoclinic volume (M_1 or M_1') with no measurable discontinuity at $P_c = 13.9(1)$ GPa. The $A_g(9)$ mode at 615 cm^{-1} and $A_g(5) + B_g(5)$ doublet at 389/393 cm^{-1} scale linearly with the octahedron volume (see Figs. S11(c) and S11(d) in the SM [92]). The apparent discontinuity in the $\nu(P)$ at P_c is due to the nonlinear pressure dependence of the oxygen octahedron volume [see Fig. 3(c)].

V. CONCLUSION

The phase diagram of VO_2 has been investigated in the past but several aspects remained unclear. Indeed, the influence of nonhydrostatic components induced either by the pressure-transmitting medium or the form of the sample (powder vs single crystal) on the phase transition led to some discrepancies. Here, we present a combined x-ray-diffraction and Raman spectroscopy investigation of high-quality VO_2 single crystal under pressure using helium as the pressure-transmitting medium. A pressure-induced soft mode is observed. This behavior is supposed to drive a transition towards an M_2 phase at pressure around 26 GPa. However, an intermediate phase transition is observed at 13.9 GPa, hindering this phonon instability. The isostructural nature of the phase transition at 13.9 GPa is confirmed experimentally. The microscopic mechanism is clarified and is based on the displacements of oxygen atoms. A phenomenological analysis based on the Landau theory of phase transition is proposed to describe the P-T phase diagram. Considering a strong anharmonic potential, the phase transitions, including the isostructural one, are described. The coupling with strains can explained the shift of the transition lines found in doped VO_2 or in thin films. At higher pressure, a phase transition to a metallic phase, probably triclinic, is observed starting from 32–35 GPa. On decompression, this phase transforms to another triclinic structure. Using high pressure allows for separating overlapping peaks at ambient conditions and brings some insights into the assignment of the different modes observed in Raman spectra. In addition, the results of the Raman spectroscopy allow relating some vibrational to different strain components or to pressure-induced microscopic variations such as the octahedron volume. This opens the opportunity to characterize the thin films in terms of structure, nature, and amplitude of strain.

ACKNOWLEDGMENTS

P.B. acknowledges the French CNRS for financial support through Grant No. Tremplin@INP2020 and C. Goujon, C. Felix, Ch. Bouchard, A. Prat, and J. Debray (CNRS, Institut Néel Grenoble) and J. Jacobs (ESRF Grenoble) for their technical help. The authors are grateful to ESRF beamline ID15B for in-house beamtime allocation. Ch. Lepoittevin (UGA Institut Néel Grenoble) and W. A. Crichton (ESRF Grenoble) are also acknowledged for their advice on crystallographic questions. L.B. acknowledges the PROCOP Mobilität Programm for financing a two-month visit in Grenoble. LN2 is a joint International Research Laboratory (IRL 3463) funded and cooperated in Canada by Université de Sherbrooke (UdS) and in France by CNRS as well as ECL, INSA Lyon, and Université Grenoble Alpes (UGA). It is also supported by the Fonds de Recherche du Québec Nature et Technologie (FRQNT).

APPENDIX: ANNEX 1

Although the active order parameter R_1^- is four components [120,121], only one single component is relevant to account for the rutile to M_1 structure distortion and becomes nonzero in the low-symmetry phase. This allows considering for R_1^--M_1 an effective phenomenological model with one-component order parameter. The R_1^- symmetry forbids odd-degree terms in a free-energy expansion, and we get a

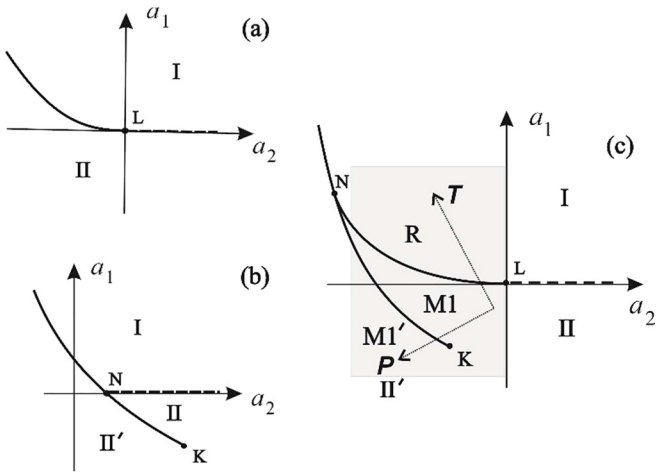

FIG. 12. Equilibrium phase diagram corresponding to free-energy equation (A1) in plane of phenomenological coefficients (a_1, a_2) for (a) canonical six-degree expansion ($a_3 > 0$, $a_4 = a_5 = 0$), (b) eight-degree potential ($a_3 < 0$, $a_4 > 0$, $a_5 = 0$), and (c) ten-degree expansion ($a_3 < 0$, $a_4 < 0$, $a_5 > 0$). (c) schematically shows "pressure (P)-temperature (T)" plane (gray area, dotted axes). Solid line: first-order; dashed: second-order phase-transition lines. L: Landau tricritical point; N: triple point; K: critical endpoint of isostructural phase transition.

canonical form for the Landau potential expanded to the tenth degree:

$$F(\eta, P, T) = a_1(P, T)\eta^2 + a_2(P, T)\eta^4 + a_3\eta^6 + a_4\eta^8 + a_5\eta^{10}. \tag{A1}$$

The mathematical analysis of the model was performed by Gufan [121], who concluded that the minimal degree of $F(\eta)$ required to describe two consecutive first-order phase transitions (here, R-M_1 and M_1-M_1') is 10 (see also Ref. [101] and references therein). This model allows to describe two low-symmetry phases. These phases have identical symmetries but differ by the magnitude of the order parameter η. Therefore, the isostructural transition is intrinsically included into this description. Figure 12 shows the evolution of the theoretical phase diagram with increasing power of the free-energy F. Thus, for VO_2 undergoing two discontinuous phase transitions, R-M_1 and M_1-M_1' [Fig. 12(c)], the phenomenological model (A1) is sufficient assuming $a_4 < 0$ and $a_5 > 0$, with M_1-M_1' phase transition being isostructural. Notice that to choose the maximal degree of expansion (between 8 and 10) the main point is the character (continuous or discontinuous) of the first transition R-M_1.

[1] F. J. Morin, Phys. Rev. Lett. **3**, 34 (1959).
[2] K. Liu, S. Lee, S. Yang, O. Delaire, and J. Wu, Mater. Today **21**, 875 (2018).
[3] Y. Ke, S. Wang, G. Liu, M. Li, T. J. White, and Y. Long, Small **14**, 1802025 (2018).
[4] R. Shi, N. Shen, J. Wang, W. Wang, A. Amini, N. Wang, and C. Cheng, Appl. Phys. Rev. **6**, 011312 (2019).
[5] W. H. Brito, M. C. O. Aguiar, K. Haule, and G. Kotliar, Phys. Rev. Lett. **117**, 056402 (2016).
[6] W. R. Mondal, E. Evlyukhin, S. A. Howard, G. J. Paez, H. Paik, D. G. Schlom, L. F. J. Piper, and W.-C. Lee, Phys. Rev. B **103**, 214107 (2021).
[7] J. B. Goodenough, J. Solid State Chem. **3**, 490 (1971).
[8] C. J. Hearn, J. Phys. C: Solid State Phys. **5**, 1317 (1972).
[9] A. Zylbersztejn and N. F. Mott, Phys. Rev. B **11**, 4383 (1975).
[10] D. Paquet and P. Leroux-Hugon, Phys. Rev. B **22**, 5284 (1980).
[11] F. Gervais and W. Kress, Phys. Rev. B **31**, 4809 (1985).
[12] S. Shin, S. Suga, M. Taniguchi, M. Fujisawa, H. Kanzaki, A. Fujimori, H. Daimon, Y. Ueda, K. Kosuge, and S. Kachi, Phys. Rev. B **41**, 4993 (1990).
[13] R. R. Andronenko, I. N. Goncharuk, V. Yu. Davydov, F. A. Chudnovskii, and E. B. Shadrin, Phys. Solid State **36**, 1136 (1994).
[14] R. M. Wentzcovitch, W. W. Schulz, and P. B. Allen, Phys. Rev. Lett. **72**, 3389 (1994).
[15] T. M. Rice, H. Launois, and J. P. Pouget, Phys. Rev. Lett. **73**, 3042 (1994).
[16] V. Eyert, Ann. Phys. **514**, 650 (2002).
[17] A. Cavalleri, Th. Dekorsy, H. H. W. Chong, J. C. Kieffer, and R. W. Schoenlein, Phys. Rev. B **70**, 161102(R) (2004).
[18] M. M. Qazilbash, M. Brehm, B.-G. Chae, P.-C. Ho, G. O. Andreev, B.-J. Kim, S. J. Yun, A. V. Balatsky, M. B. Maple, F. Keilmann, H.-T. Kim, and D. N. Basov, Science **318**, 1750 (2007).
[19] M. Netsianda, P. E. Ngoepe, C. R. A. Catlow, and S. M. Woodley, Chem. Mater. **20**, 1764 (2008).
[20] S. M. Woodley, Chem. Phys. Lett. **453**, 167 (2008).
[21] B. Lazarovits, K. Kim, K. Haule, and G. Kotliar, Phys. Rev. B **81**, 115117 (2010).
[22] V. Eyert, Phys. Rev. Lett. **107**, 016401 (2011).
[23] X. Yuan, Y. Zhang, T. A. Abtew, P. Zhang, and W. Zhang, Phys. Rev. B **86**, 235103 (2012).
[24] S. Kim, K. Kim, C.-J. Kang, and B. I. Min, Phys. Rev. B **87**, 195106 (2013).
[25] J. D. Budai, J. Hong, M. E. Manley, E. D. Specht, C. W. Li, J. Z. Tischler, D. L. Abernathy, A. H. Said, B. M. Leu, L. A. Boatner, R. J. McQueeney, and O. Delaire, Nature (London) **515**, 535 (2014).
[26] I.-H. Hwang, Z. Jin, C.-I. Park, and S.-W. Han, Sci. Rep. **7**, 14802 (2017).
[27] T. V. Slusar, J.-C. Cho, H.-R. Lee, J.-W. Kim, S. J. Yoo, J.-Y. Bigot, K.-J. Yee, and H.-T. Kim, Sci. Rep. **7**, 16038 (2017).
[28] T. J. Huffman, C. Hendriks, E. J. Walter, J. Yoon, H. Ju, R. Smith, G. L. Carr, H. Krakauer, and M. M. Qazilbash, Phys. Rev. B **95**, 075125 (2017).
[29] S. Lee, K. Hippalgaonkar, F. Yang, J. Hong, C. Ko, J. Suh, K. Liu, K. Wang, J. J. Urban, X. Zhang, C. Dames, S. A. Hartnoll, O. Delaire, and J. Wu, Science **355**, 371 (2017).
[30] S. S. Majid, D. K. Shukla, F. Rahman, S. Khan, K. Gautam, A. Ahad, S. Francoual, R. J. Choudhary, V. G. Sathe, and J. Strempfer, Phys. Rev. B **98**, 075152 (2018).
[31] T. A. Mellan, H. Wang, U. Schwingenschlögl, and R. Grau-Crespo, Phys. Rev. B **99**, 064113 (2019).

[32] F. Grandi, A. Amaricci, and M. Fabrizio, Phys. Rev. Res. **2**, 013298 (2020).

[33] S. R. Sahu, S. S. Majid, A. Ahad, A. Tripathy, K. Dey, S. Pal, B. K. De, W.-P. Hsieh, R. Rawat, V. G. Sathe, and D. K. Shukla, Phys. Rev. B **107**, 134106 (2023).

[34] D. B. McWhan, M. Marezio, J. P. Remeika, and P. D. Dernier, Phys. Rev. B **10**, 490 (1974).

[35] J. Longo and P. Kierkegaard, Acta Chem. Scand. **24**, 420 (1970).

[36] J. R. Brews, Phys. Rev. B **1**, 2557 (1970).

[37] H. Terauchi and J. B. Cohen, Phys. Rev. B **17**, 2494 (1978).

[38] Y. M. Gufan and V. P. Popov, Sov. Phys. Crystallogr. **25**, 527 (1980).

[39] Y. M. Gufan, V. P. Dmitriev, S. B. Roshal', and Y. E. Cherner, Sov. Phys.: Solid State **27**, 1046 (1985).

[40] Y. Gu, J. Cao, J. Wu, and L.-Q. Chen, J. Appl. Phys. **108**, 083517 (2010).

[41] J. Cao, Y. Gu, W. Fan, L. Q. Chen, D. F. Ogletree, K. Chen, N. Tamura, M. Kunz, C. Barret, J. Seidel, and J. Wu, Nano Lett. **10**, 2667 (2010).

[42] A. Tselev, E. Strelcov, I. A. Luk'yanchuk, J. D. Budai, J. Z. Tischler, I. N. Ivanov, K. Jones, R. Proksch, S. V. Kalinin, and A. Kolmakov, Nanoletters **10**, 2003 (2010).

[43] A. Tselev, I. A. Luk'yanchuk, I. N. Ivanov, J. D. Budai, J. Z. Tischler, E. Strelcov, A. Kolmakov, and S. V. Kalinin, Nanoletters **10**, 4409 (2010).

[44] W. Fan, J. Cao, J. Seidel, Y. Gu, J. W. Yim, C. Barrett, K. M. Yu, J. Ji, R. Ramesh, L. Q. Chen, and J. Wu, Phys. Rev. B **83**, 235102 (2011).

[45] E. Strelcov, A. Tselev, I. Ivanov, J. D. Budai, J. Zhang, J. Z. Tischler, I. Kravchenko, S. V. Kalinin, and A. Kolmakov, Nanoletters **12**, 6198 (2012).

[46] N. F. Quackenbush, H. Paik, M. J. Wahila, S. Sallis, M. E. Holtz, X. Huang, A. Ganose, B. J. Morgan, D. O. Scanlon, Y. Gu, F. Xue, L.-Q. Chen, G. E. Sterbinsky, C. Schlueter, T.-L. Lee, J. C. Woicik, J.-H. Guo, J. D. Brock, D. A. Muller, D. A. Arena, D. G. Schlom, and L. F. J. Piper, Phys. Rev. B **94**, 085105 (2016).

[47] J. P. Pouget, C.R. Phys. **22**, 37 (2021).

[48] M. Marezio, D. B. McWhan, J. P. Remeika, and P. D. Dernier, Phys. Rev. B **5**, 2541 (1972).

[49] B. L. Chamberland, J. Solid State Chem. **7**, 377 (1973).

[50] J. P. Pouget, H. Launois, T. M. Rice, P. Dernier, A. Gossard, G. Villeneuve, and P. Hagenmuller, Phys. Rev. B **10**, 1801 (1974).

[51] J. P. Pouget and H. Launois, J. de Physique Colloques **37**, C4-49 (1976).

[52] M. Ghedira, H. Vincent, M. Marezio, and J. C. Launay, J. Solid State Chem. **22**, 423 (1977).

[53] J. P. Pouget, H. Launois, J. P. D'Haenens, P. Merenda, and T. M. Rice, Phys. Rev. Lett. **35**, 873 (1975).

[54] J. Galy and G. Miehe, Solid State Science **1**, 433 (1999).

[55] A. C. Jones, S. Berweger, J. Wei, D. Cobden, and M. B. Raschke, Nano Lett. **10**, 1574 (2010).

[56] H. Guo, K. Chen, Y. Oh, K. Wang, C. Dejoie, S. A. Syed Asif, O. L. Warren, Z. W. Shan, J. Wu, and A. M. Minor, Nanoletters **11**, 3207 (2011).

[57] J. M. Atkin, S. Berweger, E. K. Chavez, M. B. Raschke, J. Cao, W. Fan, and J. Wu, Phys. Rev. B **85**, 020101 (2012).

[58] J. H. Park, J. M. Coy, T. S. Kasirga, C. Huang, Z. Fei, S. Hunter, and D. H. Cobden, Nature (London) **500**, 431 (2013).

[59] J. D. Budai, A. Tselev, J. Z. Tischler, E. Strelcov, A. Kolmakov, W. J. Liu, A. Gupta, and J. Narayan, Acta Mater. **61**, 2751 (2013).

[60] M. Liu, A. J. Sternbach, M. Wagner, T. V. Slusar, T. Kong, S. L. Bud'ko, S. Kittiwatanakul, M. M. Qazilbash, A. McLeod, Z. Fei, E. Abreu, J. Zhang, M. Goldflam, S. Dai, G.-X. Ni, J. Lu, H. A. Bechtel, M. C. Martin, M. B. Raschke, R. D. Averitt, S. A. Wolf, H.-T. Kim, P. C. Canfield, and D. N. Basov, Phys. Rev. B **91**, 245155 (2015).

[61] H. Kim, T. V. Slusar, D. Wulferding, I. Yang, J.-C. Cho, M. Lee, H. C. Choi, Y. H. Jeong, H.-T. Kim, and J. Kim, Appl. Phys. Lett. **109**, 233104 (2016).

[62] M. Liu, S. Xie, L. Wei, M. Galluzzi, Y. Li, Q. Wang, X. Zhou, Y. Wang, J. Li, Acta Mater. **195**, 720 (2020).

[63] J. Cao, E. Ertekin, V. Srinivasan, W. Fan, S. Huang, H. Zheng, J. W. L. Yim, D. R. Khanal, D. F. Ogletree, J. C. Grossman, and J. Wu, Nat. Nanotechnol. **4**, 732 (2009).

[64] N. B. Aetukuri, A. X. Gray, M. Drouard, M. Cossale, L. Gao, A. H. Reid, R. Kukreja, H. Ohldag, C. A. Jenkins, E. Arenholz, K. P. Roche, H. A. Dürr, M. G. Samant, and S. S. P. Parkin, Nat. Phys. **9**, 661 (2013).

[65] S. Kittiwatanakul, S. A. Wolf, and J. Lu, Appl. Phys. Lett. **105**, 073112 (2014).

[66] E. Arcangeletti, L. Baldassarre, D. Di Castro, S. Lupi, L. Malavasi, C. Marini, A. Perucchi, and P. Postorino, Phys Rev Lett. **98**, 196406 (2007).

[67] C. Marini, E. Arcangeletti, D. Di Castro, L. Baldassare, A. Perucchi, S. Lupi, L. Malavasi, L. Boeri, E. Pomjakushina, K. Conder, and P. Postorino, Phys. Rev. B **77**, 235111 (2008).

[68] C. Marini, L. Baldassarre, M. Baldini, A. Perucchi, D. Di Castro, L. Malavasi, S. Lupi, and P. Postorino, High Pressure Res. **30**, 55 (2010).

[69] H. Zhang, Q. Li, B. Cheng, Z. Guan, R. Liu, B. Liu, Z. Liu, X. Li, T. Cui, and B. Liu, RSC Adv. **6**, 104949 (2016).

[70] X. Zhang, J. Zhang, F. Ke, G. Li, Y. Ma, X. Liu, C. Liu, Y. Han, Y. Ma, and C. Gao, RSC Adv. **5**, 54843 (2015).

[71] L. Bai, Q. Li, S. A. Corr, Y. Meng, C. Park, S. V. Sinogeikin, C. Ko, J. Wu, and G. Shen, Phys. Rev. B **91**, 104110 (2015).

[72] M. Mitrano, B. Maroni, C. Marini, M. Hanfland, B. Joseph, P. Postorino, and L. Malavasi, Phys. Rev. B **85**, 184108 (2012).

[73] V. Balédent, T. T. F. Cerqueira, R. Sarmiento-Pérez, A. Shukla, C. Bellin, M. Marsi, J.-P. Itié, M. Gatti, M. A. L. Marques, S. Botti, and J.-P. Rueff, Phys. Rev. B **97**, 024107 (2018).

[74] Q. Li, H. Zhang, C. Lin, F. Tian, J. S. Smith, C. Park, B. Liu, and G. Shen, J. Alloys Compd. **709**, 260 (2017).

[75] M. Baldini, P. Postorino, L. Malavasi, C. Marini, K. W. Chapman, and H.-K. Mao, Phys. Rev. B **93**, 245137 (2016).

[76] H. He, H. Gao, W. Wu, S. Cao, J. Hong, D. Yu, G. Deng, Y. Gao, P. Zhang, H. Luo, and W. Ren, Phys. Rev. B **94**, 205127 (2016).

[77] H. Zhang, Q. Li, F. Wang, R. Liu, Y. Mao, Z. Liu, X. Li, K. Yang, T. Cui, and B. Liu, J. Phys. Chem. C **123**, 955 (2019).

[78] S.-Y. Xie, L. Wang, F. Liu, X.-B. Li, L. Bai, V. B. Prakapenka, Z. Cai, H.-K. Mao, S. Zhang, and H. Liu, J. Phys. Chem. Lett. **9**, 2388 (2018).

[79] H. Zhang, Z. Guan, B. Cheng, Q. Li, R. Liu, J. Zhang, Z. Liu, K. Yang, T. Cui, and B. Liu, RSC Adv. **7**, 31597 (2017).

[80] Y. Chen, S. Zhang, F. Ke, C. Ko, S. Lee, K. Liu, B. Chen, J. W. Ager, R. Jeanloz, V. Eyert, and J. Wu, Nano Lett. **17**, 2512 (2017).

[81] Y. Bando, M. Kyoto, T. Takada, and S. Muranaka, J. Cryst. Growth **45**, 20 (1978).

[82] W. B. Holzapfel, J. Appl. Phys. **93**, 1813 (2003).

[83] K. Takemura, J. Appl. Phys. **89**, 662 (2001).

[84] A. Dewaele and P. Loubeyre, High Pressure Res. **27**, 419 (2007).

[85] A. Dewaele, P. Loubeyre, and M. Mezouar, Phys. Rev. B **70**, 094112 (2004).

[86] C. Prescher and V. B. Prakapenka, High Pressure Res. **35**, 223 (2015).

[87] M. Wojdyr, J. Appl. Crystallogr. **43**, 1126 (2010).

[88] *Oxford Diffraction CrysAlisPRO* (Agilent Technologies UK Ltd, Yarnton, England).

[89] V. Petricek, M. Dusek, and L. Palatinus, Z. fur Kristallogr. Crystalline Materials **229**, 345 (2014).

[90] K. Momma and F. Izumi, J. Appl. Crystallogr. **44**, 1272 (2011).

[91] J. Rodriguez-Carvajal, Physica B **192**, 55 (1993).

[92] See Supplemental Material at http://link.aps.org/supplemental/10.1103/PhysRevB.108.144106 for additional x-ray and Raman data.

[93] A. G. Aronov, D. N. Mirlin, I. I. Reshina, and F. A. Chudnovskii, Sov. Phys. Solid State **19**, 110 (1977).

[94] P. Schilbe, Physica B **316-317**, 600 (2002).

[95] P. Schilbe and D. Maurer, Mater. Sci. Eng. A **370**, 449 (2004).

[96] J. Y. Chou, J. L. Lensch-Falk, E. R. Hemesath, and L. J. Lauhon, J. Appl. Phys. **105**, 034310 (2009).

[97] M. Zaghrioui, J. Sakai, N. H. Azhan, K. Su, and K. Okimura, Vib. Spectrosc. **80**, 79 (2015).

[98] K. Shibuya and A. Sawa, J. Appl. Phys. **122**, 015307 (2017).

[99] X. Yuan, W. Zhang, and P. Zhang, Phys. Rev. B **88**, 035119 (2013).

[100] R. Basu, A. Patsha, S. Chandra, S. Amirthapandian, R. K. Gururaj, A. Dasgupta, and S. Dhara, J. Phys. Chem. C **123**, 11189 (2019).

[101] V. Dmitriev, *Discontinuous Phase Transitions in Condensed Matter* (World Scientific, Singapore, 2023).

[102] H.-T. Kim, Y. W. Lee, B.-J. Kim, B.-G. Chae, S. J. Yun, K.-Y. Kang, K.-J. Han, K.-J. Yee, and Y.-S. Lim, Phys. Rev. Lett. **97**, 266401 (2006).

[103] Z. Tao, T.-R. T. Han, S. D. Mahanti, P. M. Duxbury, F. Yuan, C.-Y. Ruan, K. Wang, and J. Wu, Phys. Rev. Lett. **109**, 166406 (2012).

[104] J. Laverock, S. Kittiwatanakul, A. A. Zakharov, Y. R. Niu, B. Chen, S. A. Wolf, J. W. Lu, and K. E. Smith, Phys. Rev. Lett. **113**, 216402 (2014).

[105] D. Lee, B. Chung, Y. Shi, G.-Y. Kim, N. Campbell, F. Xue, K. Song, S.-Y. Choi, J. P. Podkaminer, T. H. Kim, P. J. Ryan, J.-W. Kim, T. R. Paudel, J.-H. Kang, J. W. Spinuzzi, D. A. Tenne, E. Y. Tsymbal, M. S. Rzchowski, L. Q. Chen, J. Lee, and C. B. Eom, Science **362**, 1037 (2018).

[106] S. Zhang, J. Y. Chou, and L. Lauhon, Nano Lett. **9**, 4527 (2009).

[107] S.-J. Chang, W.-K. Hong, H. J. Kim, J. B. Lee, J. Yoon, H. C. Ko, and Y. S. Huh, Nanotechnology **24**, 345701 (2013).

[108] S.-J. Chang, J. B. Park, G. Lee, H. J. Kim, J.-B. Lee, T.-S. Bae, Y.-K. Han, T. J. Park, Y. S. Huh, and W.-K. Hong, Nanoscale **6**, 8068 (2014).

[109] K. Okimura, N. H. Ashan, T. Hajiri, S.-I. Kimura, M. Zaghrioui, and J. Sakai, J. Appl. Phys. **115**, 153501 (2014).

[110] E. Evlyukhin, S. A. Howard, H. Paik, G. J. Paez, D. J. Gosztola, C. N. Singh, D. G. Schlom, W.-C. Lee, and L. F. J. Piper, Nanoscale **12**, 18857 (2020).

[111] R. Srivastava and L. L. Chase, Phys. Rev. Lett. **27**, 727 (1971).

[112] B. Y. Qu, H. Y. He, and B. C. Pan, J. Appl. Phys. **110**, 113517 (2011).

[113] S. Wall, S. Yang, L. Vidas, M. Chollet, J. M. Glownia, M. Kozina, T. Katayama, T. Henighan, M. Jiang, T. A. Miller, D. A. Reis, L. A. Boatner, O. Delaire, and M. Trigo, Science **362**, 572 (2018).

[114] C. W. Rischau, X. He, G. Mazza, S. Gariglio, J.-M. Triscone, P. Ghosez, and J. del Valle, Phys. Rev. B **107**, 115139 (2023).

[115] E. Strelcov, A. Ievlev, A. Belianinov, A. Tselev, A. Kolmakov, and S. V. Kalinin, Sci. Rep. **6**, 29216 (2016).

[116] P. Shvets, O. Dikaya, K. Maksimova, and A. Goikhman, J. Raman Spectrosc. **50**, 1226 (2019).

[117] R. Basu, V. Srihari, M. Sardar, S. K. Srivastava, S. Bera, and S. Dhara, Sci. Rep. **10**, 1977 (2020).

[118] P. Shvets, K. Maksimova, and A. Goikhman, J. Appl. Phys. **129**, 055302 (2021).

[119] J. Li, L. Wu, S. Yang, X. Jin, W. Wang, J. Tao, L. Boatner, M. Babzien, M. Fedurin, M. Palmer, W. Yin, O. Delaire, and Y. Zhu, Phys. Rev. X **12**, 021032 (2022).

[120] Y. M. Gufan and V. P. Dmitiev, Sov. Phys. Crystallogr. **25**, 6 (1980).

[121] Y. M. Gufan, *Structural Phase Transitions* (Moscow, Izdatel'stvo Nauka, 1982).